Automated Landslide Mapping with Open-Source Satellite Data in GEE: A Sri Lankan Case Study.

Lasantha HS
Geology Division
Geological Survey and Mines Bureau,
Sri Lanka.
https://orcid.org/0009-0003-5397-4511

Prasanna R
The Joint Centre for Disaster Research,
Massey University,
New Zealand..
https://orcid.org/0000-0002-5608-6558

Madusanka DAG
National Building Research Institute,
Sri Lanka.
madusankakkc@gmail.com

Abstract

Rainfall-induced landslides are the most frequent natural hazards in Sri Lanka. This study developed a scalable, cloud-based landslide detection method that integrates satellite data, topographic parameters, and a machine learning framework implemented on Google Earth Engine (GEE) to support rapid, reliable landslide mapping in disaster scenarios and data-scarce regions. The methodology was applied to the central highlands and the south-western parts of Sri Lanka. Multi-temporal Sentinel-1 and Sentinel-2 images, along with a 12.5 m digital elevation model, were used to generate four composite datasets (M1–M4) for pixel-based classification. M1 includes spectral index differences between pre-event and post-event optical images, M2 incorporates spectral distance and spectral angle data, M3 contains topographic attributes, and M4 combines all datasets with synthetic aperture radar (SAR) amplitude ratio bands. Inter-area model training and validation were conducted using RF, CART, SVM, and GTB with independent datasets from study area-1, followed by transferability testing in a second area. Model performance was evaluated using overall accuracy, Precision, Recall, F1-Score, Kappa, and AUC. SVM-M4 performed best in inter-area analysis, while GBT–M4 and CART–M3 showed superior transferability. Cloud contamination and false detections remained key challenges.

Keywords

Landslides, GEE, Machine-learning, GTB, CART, RF, SVM DEM, satellite images

I. Introduction

Landslides rank among the top natural hazards worldwide, causing significant damage to people, infrastructure, and the economy [1]-[4]. They are naturally triggered by intense rainfall, seismic activity, and rapid snowmelt [5]-[8]. Since landslides continue to affect both developed and developing regions, there is growing interest in identifying effective methods to assess and reduce landslide risk [2],[9],[10]. Reliable landslide mapping is essential for supporting landslide risk modelling and hazard assessment, facilitating quick disaster responses by identifying vulnerable areas, and promoting long-term planning and the implementation of landslide mitigation measures [9],[11],[12].

Landslides during the monsoon season are among the most life-threatening natural hazards in Sri Lanka, causing annual loss of life and severe infrastructure damage [13]. The increasing frequency and intensity of such events underscore the urgent need for rapid, reliable landslide-detection methodologies. This need becomes even more critical during extreme weather events, such as Cyclone Dithwa in 2025, which triggered thousands of landslides within a short period, severely disrupting transportation, communication, and power infrastructure "unpublished" [14]. Under these conditions, conventional field-based landslide identification becomes impractical and cannot be afforded by national agencies like the National Building Research Institute (NBRI), given limited expert personnel, underscoring the need to develop automated, large-scale, and near-real-time landslide detection approaches to support timely decision-making and effective disaster response.

Hence, the present study was designed to examine two landslide-prone areas in Sri Lanka using freely available satellite imagery in Google Earth Engine (GEE). The study integrates widely used machine learning algorithms, including Random Forest (RF), Classification and Regression Trees (CART), Support Vector Machine (SVM), and Gradient Tree Boosting (GTB), using independent training and validation datasets. Both intra-area performance and model transferability across geographically distinct regions were examined. Model performance was evaluated using standard metrics, and the best-performing models are recommended for reliable, scalable landslide detection.

II. Literature Review

Conventional field-based techniques are often time-consuming, labour-intensive, and limited in spatial coverage, particularly in remote or hard-to-reach areas, which limits their effectiveness for large-scale, rapid assessments [8],[15]-[17]. Hence, landslide mapping methods have evolved towards advanced remote sensing technologies, such as automated, data-driven, satellite-image-based deep learning techniques for landslide detection [12], [18]-[20].

Recent studies have increasingly highlighted the development of reliable and cost-effective landslide detection methods using open-access datasets, and global landslide monitoring has been significantly improved through the rise of cloud-based geospatial platforms and open data infrastructures, such as Google Earth Engine (GEE) and Sentinel Hub[3],[8],[21]-[25].

GEE enables efficient processing of multi-temporal satellite data through a web-based interface, eliminating the need for high-end local computing infrastructure [21], [23]. It supports large-scale data processing and rapid analysis, facilitating advanced techniques such as machine learning–based classification [21],[23],[26]-[27].

Widely used satellite datasets for landslide detection include Sentinel-1 and Sentinel-2, while common machine learning techniques include Random Forest (RF), Gradient Tree Boosting (GTB), Support Vector Machine (SVM), Naïve Bayes (NB), and Classification and Regression Trees (CART)[12],[18],[19]. Most studies adopt a bi-temporal

https://doi.org/10.54389/ROOS2184

approach, using pre-event and post-event imagery to derive spectral indices and perform change detection for landslide identification [12],[18],[20],[21],[28]. Additionally, topographic variables such as elevation, slope, aspect, profile vertical) curvature, and plan (horizontal) curvature are frequently incorporated to enhance model performance. However, in many cases, the same dataset is used for both training and validation, often via random splitting such as 70:30 or 80:20 [18]-[20], which can lead to biased performance estimates. Furthermore, the generalisation ability of machine learning models, especially their transferability across different geographic regions and time periods, has been only limitedly explored in existing studies[19].

Sri Lanka, a tropical island in the Indian Ocean, where Rainfall-induced landslides are among the most critical natural hazards in the country, causing significant impacts on human life and infrastructure, particularly during the Southwest and Northeast monsoon seasons and inter-monsoonal periods [6],[29]-[31]. Hilly regions such as the central highlands of Sri Lanka frequently experience landslides, and Badulla, Galle, Hambantota, Kandy, Kalutara, Kegalle, Matale, Matara, Nuwara Eliya, and Ratnapura are the most severely affected, landslide-prone districts [5].

The National Building Research Institute (NBRI), Sri Lanka's primary agency for landslide risk management, plays a key role in detection, monitoring, hazard zonation, and mitigation[31]-[33]. However, while NBRI maintains inventories of major landslides in populated areas, events in remote or uninhabited regions often remain undocumented, leading to critical gaps in hazard assessment, long-term planning, and disaster risk reduction[34].

Additionally, several studies have been conducted on landslides, with the majority focusing on susceptibility mapping, hazard zonation, impact assessment, and detailed analysis of individual landslides or small areas [6],[35]-[41]. Although some studies have utilised satellite imagery for landslide detection, these efforts have largely concentrated on individual large-scale events [42]-[44]. Only a few studies have conducted landslide susceptibility mapping at regional scales using advanced techniques, such as satellite imagery integrated with machine learning [34], [44].

GEE has been successfully applied in Sri Lanka for applications such as flood mapping, crop disease monitoring, and forest cover change detection [45]-[47]. However, few studies have integrated GEE, satellite imagery, and machine learning for landslide detection. [44].

Considering the above knowledge gaps, this study was designed to address these limitations by implementing the following methodology.

III. Methodology

For this research, two landslide-prone regions in Sri Lanka were selected as the study area (Fig. 1). The terrain is mainly mountainous, underlain by fractured, weathered high-grade metamorphic basement rocks and residual soil profiles developed through intense tropical weathering. The region experiences heavy rainfall influenced by the Southwest monsoon (May to September) and inter-monsoonal convectional rainfall, mainly during October and November, with average annual rainfall ranging from 2,500 mm to 5,000 mm[31], [45].

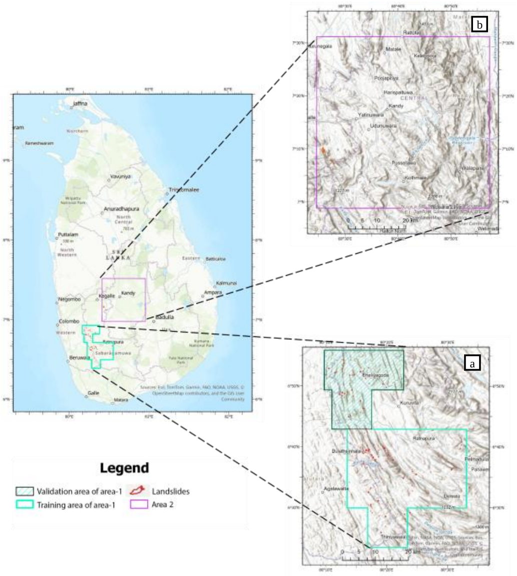

Fig. 1. The maps of the study area a) area-1, b) area-2.

The workflow of this study comprises three main phases, namely data collection and pre-processing, machine learning model training and evaluation, and susceptibility modelling (Fig. 2).

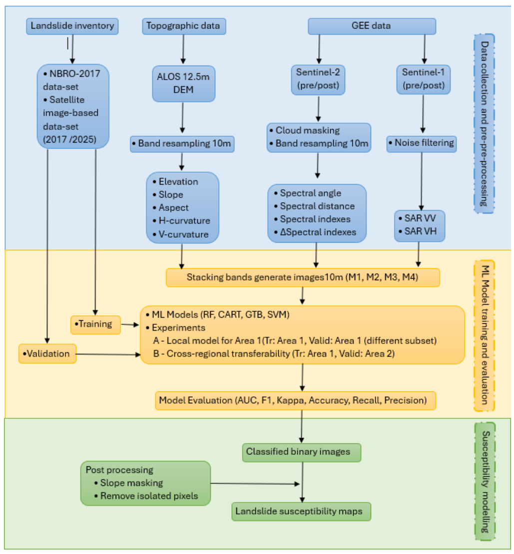

Fig. 2. The methodological workflow of the study.

In the first phase, a historical landslide inventory was created for the study area, covering the periods from 2017 to 2018 and from June 2025 to February 2026 (Fig. 2). This inventory was compiled from reports by the National Building Research Institute (NBRI) [48], supplemented by visual interpretation of high-resolution satellite imagery and identification of historical landslide scars in Google Earth

Pro. Then, a 12.5m resolution digital elevation model (DEM) was incorporated [49] to extract topographic parameters (Fig. 2).

In 2017, based on NBRI records and satellite-based rainfall analyses, the highest precipitation occurred on 25 May 2017, triggering widespread slope failures during that period [48]. Therefore, for study area-01, a pre-event period from 01 January 2017 to 12 May 2017, and a post-event period from 12 June 2017 to 01 January 2018 were taken. These intervals were chosen to minimize cloud contamination and effectively capture the immediate aftermath of the landslide-triggering rainfall event. Similarly, in 2025, during the storm Ditwa (28 November 2025 to 30 November 2025), Sri Lanka recorded the heaviest precipitation in the last 30 years. This triggered the more than 3000 landslides in Sri Lanka “unpublished” [14]. Therefore, for the study area, the period from 20 June to 28 November and from 05 December 2025 to 26 February 2026 was considered as the pre-event and post-event periods, respectively. Freely available Sentinel-2 data corresponding to the selected time periods were obtained from GEE.

To reduce Cloud contamination, a machine-learning–based cloud-masking approach, Cloud Score+ (CS+), available in the GEE platform [50], was employed. Cloud-filtered median composites of Sentinel-2 imagery were generated for both the pre-event and post-event periods in both study areas (Fig. 2) to further reduce residual cloud contamination and improve image reliability. To ensure consistency across all spectral layers, Sentinel-2 imagery was resampled to 10 m resolution using bilinear resampling in Google Earth Engine (GEE). These composites served as the primary input for the analyses.

Four Sentinel-1 ground range detected (GRD) products were acquired from the Copernicus data hub, representing the same pre-event and post-event periods in interferometric wide (IW) swath mode and descending orbit configuration. Standard pre-processing was performed to enhance image quality and reduce noise using the SNAP (Sentinel Application Platform) software.

To spectral changes associated with landslides, Euclidean spectral distance (ESD) and spectral angle mapper (SAM) [51], [52] were computed using the pre-event and post-event Sentinel-2 composite images, and the resulting band differences were stored as separate image bands. Additionally, a set of spectral indices, including the normalized difference vegetation index (NDVI, enhanced vegetation index (EVI), soil adjusted vegetation index (SAVI), normalized Difference Water Index (NDWI), Modified Normalized Difference Water Index (MNDWI), Built-up Index(BI), Normalized Difference Built-up Index (NDBI), Bare Soil Index (BSI), and Shortwave Infrared Ratio Index (SWIRI)was calculated from the composite images using the corresponding spectral bands defined for each index[8],[12],[22][53]. Index differences(∆) were calculated by subtracting pre-event from post-event values, and the resulting layers were stored as additional image bands.

The 12.5 m Digital Elevation Model (DEM) was resampled to 10 m spatial resolution, and using ArcGIS Pro, five topographic parameters, including elevation, slope, aspect, profile curvature, and tangent curvature, were derived and stored as separate image bands for subsequent analysis. Pre-event and post-event Sentinel-1 SAR composites were used to compute the amplitude ratio for both VV and VH polarizations. The calculated values were stored as two separate image bands for subsequent analysis.

Finally, four image sets were generated by stacking the computed bands as M1, M2, M3, and M4 (Table I).

The machine learning-based classification was tested in two scenarios, experiment A and experiment B.

TABLE I. BAND COMPOSITION OF IMAGES.

Image	Band Composition
M1	∆NDVI, ∆EVI, ∆SAVI, ∆NDWI, ∆MNDWI, ∆BI, ∆NDBI, ∆BSI, ∆SWIRI
M2	M1, ∆Spectral_angle, ∆Spectral_distance
M3	M2, Elevation, Slope, Aspect, Profile curvature, and Tangent curvature
M4	M3, ∆VH, ∆VV, ∆(VH/VV)

Experiment A was conducted to evaluate model accuracy under ideal conditions and to assess baseline model performance. For this study, area-1 was selected, and shaded area was used for model validation, while the remaining area was used for training (Fig. 1a). All 4 methods were applied with 4 images, and their performance was evaluated on the validation dataset.

To assess the model's transferability and generalisation across different regions and time periods, experiment B was designed and conducted. The same dataset used in experiment A was used for training, while area-2 with the 2025 landslide dataset was used for validation, and performance was evaluated.

Across experiments, the models' performance was assessed using overall accuracy (OA), F1 score, receiver operating characteristic (ROC) curve, area under the curve (AUC), and confusion matrices. Finally, classified images were processed by applying a slope mask and removing isolated pixels, and the final landslide susceptibility maps were created.

IV. RESULTS

Experiment A

The performance of the machine learning models under intra-area validation conditions is shown in Table II.

TABLE II. RESULTS OF EXPERIMENT A

ML Model	OA	Kappa	Precision	Recall	F1-Score	AUC
RF-A-M1	0.8488	0.6975	0.9592	0.7285	0.8281	0.9264
RF-A-M2	0.8503	0.7005	0.9636	0.7280	0.8294	0.9289
RF-A-M3	0.8660	0.7320	0.9828	0.7450	0.8476	0.9495
RF-A-M4	0.8625	0.7250	0.9840	0.7370	0.8428	0.9485
GTB-A-M1	0.8390	0.6779	0.9606	0.7070	0.8145	0.9193
GTB-A-M2	0.8398	0.6795	0.9651	0.7050	0.8148	0.9165
GTB-A-M3	0.8708	0.7415	0.9837	0.7540	0.8537	0.9533
GTB-A-M4	0.8685	0.7370	0.9849	0.7485	0.8506	0.9493
SVM-A-M1	0.8428	0.6855	0.9647	0.7115	0.8190	0.9247
SVM-A-M2	0.8448	0.6895	0.9631	0.7170	0.8220	0.9288
SVM-A-M3	0.8703	0.7405	0.9799	0.7560	0.8535	0.9435
SVM-A-M4	0.8738	0.7475	0.9770	0.7655	0.8584	0.9437
CART-A-M1	0.8478	0.6955	0.9537	0.7310	0.8276	0.9217
CART-A-M2	0.8473	0.6945	0.9590	0.7255	0.8261	0.9214
CART-A-M3	0.8665	0.7330	0.9741	0.7530	0.8494	0.9333
CART-A-M4	0.8640	0.7280	0.9667	0.7540	0.8472	0.9327

Experiment A assesses the models' predictive ability when both the training and validation datasets come from area-1. Overall, the models exhibit high predictive performance, with overall accuracy (OA) ranging from 0.8390 to 0.8738, F-1 scores from 0.8145 to 0.8584, and AUC values from 0.9165 to 0.9533 (Table II).

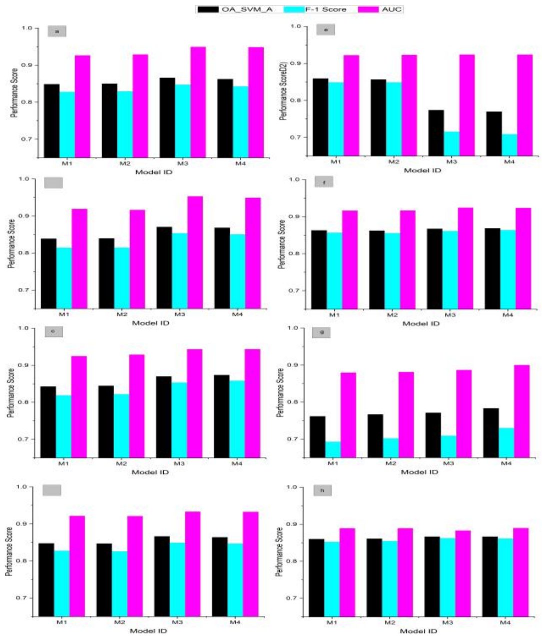

Fig. 3. Model performance across experiments: a) A-RF, b) A-GTB, c) A-SVM, d) A-CART, e) B-RF, f) B-GTB, g) B-SVM, h) B-CART

Among the evaluated models, SVM-A-M4 achieved the highest overall accuracy (OA = 0.8738) and Kappa coefficient (0.7475), indicating the strongest agreement between predicted and observed landslide occurrences (Fig. 3c, Table II). Precision values across all models are consistently high (0.9537–0.9849), indicating that most predicted landslide pixels correspond to actual landslide events. However, recall values range from 0.7050 to 0.7655, suggesting that some landslide occurrences remain undetected (Table II).

The F1-score, which balances precision and recall, varies from 0.8145 to 0.8584, with SVM-A-M4 achieving the highest F1-score (0.8584) (Fig. 3c, Table II). Figure 4 further confirms the performance of the optimal model with actual representations, which are verified by high-resolution satellite images (Fig. 4b,c,f,g,i,j,k,l,m,n,o,p,q,r,s,t,u,v). These results indicate that models perform very effectively when applied to the same spatial domain used for training.

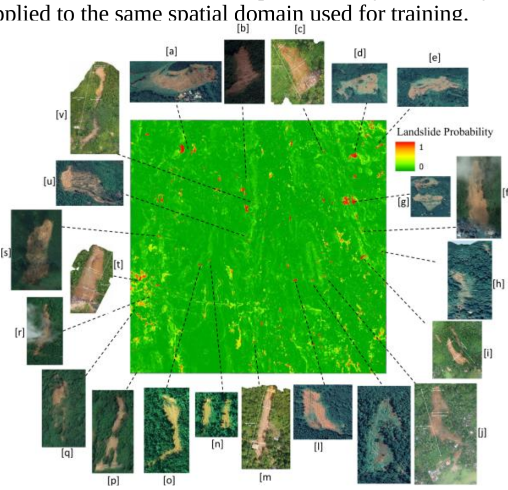

Fig. 4. Verification of landslide detections on area-1 with historical landslide inventories and high-resolution satellite imageries.

The ROC curves for Experiment A demonstrate strong predictive capability for most machine learning models, with AUC values exceeding 0.90. GTB-A-M3 achieved the highest prediction accuracy, with an AUC of 0.953, indicating excellent discrimination between landslide and non-landslide locations (Fig. 3b, Table II).

The results show that all machine learning techniques in this test demonstrate continuous improvement from M1 to M3; however, there is a slight decrease in model performance after SAR image data (M4) across all models(Fig. 3).

Experiment B

Experiment B assesses model transferability by applying models trained in area-1 to predict landslide susceptibility in area-2. This experiment is crucial for assessing the models' transferability, and the results are presented in Table III.

TABLE III. RESULTS OF EXPERIMENT B

ML Model	OA	Kappa	Precision	Recall	F1-Score	AUC
RF-B-M1	0.8595	0.7190	0.9095	0.7961	0.8490	0.9225
RF-B-M2	0.8568	0.7135	0.8971	0.8060	0.8491	0.9230
RF-B-M3	0.7743	0.5485	0.9652	0.5690	0.7159	0.9239
RF-B-M4	0.7700	0.5400	0.9647	0.5605	0.7090	0.9240
GTB-B-M1	0.8630	0.7260	0.8980	0.8190	0.8567	0.9163
GTB-B-M2	0.8623	0.7235	0.8992	0.8160	0.8556	0.9165
GTB-B-M3	0.8673	0.7345	0.9033	0.8225	0.8610	0.9243
GTB-B-M4	0.8688	0.7375	0.8989	0.8310	0.8636	0.9234
SVM-B-M1	0.7618	0.5235	0.9729	0.5385	0.6933	0.8796
SVM-B-M2	0.7670	0.5340	0.9726	0.5495	0.7022	0.8815
SVM-B-M3	0.7715	0.5430	0.9738	0.5580	0.7095	0.8869
SVM-B-M4	0.7835	0.5670	0.9694	0.5855	0.7300	0.9001
CART-B-M1	0.8600	0.7200	0.9018	0.8080	0.8523	0.8893
CART-B-M2	0.8610	0.7220	0.8954	0.8175	0.8547	0.8893
CART-B-M3	0.8665	0.7330	0.8895	0.8370	0.8624	0.8830
CART-B-M4	0.8665	0.7330	0.8945	0.8310	0.8616	0.8898

The overall accuracy values range from 0.7618 to 0.8688, the F1-score values range from 0.6933 to 0.8636, and the AUC values range from 0.8796 to 0.9243. The best performance is observed for GTB-B-M4, which achieved the highest overall accuracy (OA = 0.8688), Kappa coefficient (0.7375), and F1-score (0.8636)(Fig. 3b, Table III).Fig. 5 further confirms the performance of the optimal model with actual representations, which are verified by high-resolution satellite images (Fig. 5a, b, c, d, e, f, g, j, k, l, m, n, o, p, q). capability even when applied to a different geographic area. Similarly, CART-B-M3 performs competitively, with an OA of 0.8665 and an F1-score of 0.8624, suggesting good transferability. In this test, the GTB method demonstrates continuous model improvement from M1 to M3, with a slight drop after M4 (Fig. 3).

In contrast, SVM exhibits significantly lower performance, with OA values ranging from 0.7618 to 0.7835 and F1-scores ranging from 0.6933 to 0.7300(Fig. 3, Table III). Although precision values remain high (>0.97), recall values are relatively low, indicating that many landslide occurrences were not detected. The results suggest that RF and SVM models trained in area-1 do not fully capture the geological and geomorphological characteristics of area-2, resulting in lower predictive accuracy.

V. DISCUSSION

All machine learning models used in this study were developed following a systematic preprocessing and optimization workflow to ensure robust and reliable landslide prediction. Furthermore, hyperparameter tuning was applied to each machine learning algorithm to enhance model performance and avoid sub-optimal configurations.

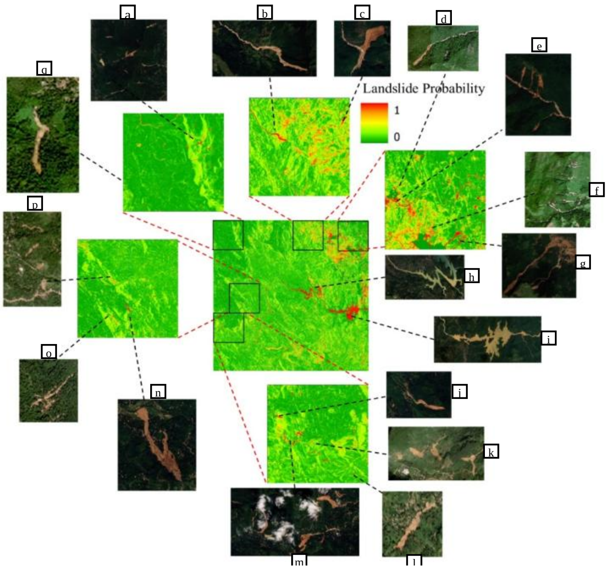

Fig. 5. Verification of landslide detections on area-2 with historical landslide inventories and high-resolution satellite imageries.

The results of experiment A indicate that all 4 machine learning techniques exhibit high predictive performance, with overall accuracy in intra-area analysis. The SVM-A–M4 was the best-performing model for inter-area landslide detection, followed by GTB-A-M3; both RF and CART performed similarly (Fig. 3).

This study uses an independent dataset for training and calibration, providing a more robust and realistic assessment of the model's generalization capability than widely applied random partitioning of a single dataset into training and validation subsets, such as 70:30 or 80:20.

All machine learning models in Test A demonstrate a systematic improvement from M1 to M3 (Fig. 3). This trend is consistent with previous findings by Yang and others, which indicate that incorporating additional spectral, topographic, and change-detection features can significantly enhance classification performance[12].

Experiment B evaluates the spatiotemporal transferability of the applied machine learning models. The results suggest that GTB-B-M4 and CART-B-M3 perform best and are similar to those reported by Peter and others [19], thereby verifying model transferability and supporting our findings.

However, a noticeable reduction in performance was observed for the SVM and RF models (Fig. 3). This decline can be attributed to a domain shift between the training and validation datasets, in which variations in environmental conditions, optical imagery, SAR backscatter responses, and terrain characteristics alter the underlying data distributions. SVM, which relies on defining an optimal decision boundary, is particularly sensitive to such distributional changes, leading to reduced generalisation. Similarly, RF, despite its robustness, tends to rely on patterns learned from the training data and may struggle when exposed to unseen conditions.

In contrast, GTB and CART demonstrated comparatively stable performance under transfer conditions (Fig. 3). GTB, through its sequential learning strategy, effectively captures complex, nonlinear relationships and adapts more effectively to subtle variations in predictor variables. CART, although simpler, establishes threshold-based decision rules that are often physically meaningful and remain relatively consistent across different regions. These findings highlight that models with adaptive learning mechanisms and interpretable decision structures exhibit superior transferability in landslide susceptibility mapping, particularly in heterogeneous and non-stationary environments.

Overall, experiment A suggests that all applied methods can be reliably used to accurately model landslide susceptibility within the same geographic region. while Trees GTB and CART depict comparatively stable and better performance under transfer conditions.

Across the experiments, GTB consistently demonstrates strong and stable performance, achieving the best transferability in Experiment B. Furthermore, the GTB techniques show consistent performance across M1-M3, with a slight drop at M4 in experiments A and B. In contrast, SVM exhibits strong performance in Experiment A but significantly lower transferability in Experiment B, suggesting sensitivity to spatial data variations.

B. Challenges of the current study.

Despite the promising outcomes of this study, several challenges emerged, including cloud contamination and false detections in agricultural areas and on exposed soil surfaces, as well as muddy water in streams and reservoirs.

Clouds pose a major challenge for the use of optical satellite imagery, particularly for accurately interpreting surface features such as landslides, which are especially critical in tropical and mountainous regions like Sri Lanka[8],[27],[54]. This study used the Cloud Score+ algorithm in Google Earth Engine, which assigns a cloud probability score to each pixel based on spectral properties[50] to mitigate cloud contamination. By applying a suitable threshold, high-probability cloud pixels were masked. Then, multiple images were stacked to create a median composite, which calculates the median reflectance value per pixel. reducing residual noise from thin clouds, haze, and lighting inconsistencies, and producing a more stable and representative land surface image for classification and change detection. However, it masked not only thick clouds but also thin clouds, their fringes, and neighbouring pixels, resulting in the loss of useful surface data and a reduction in the effective analysis area. Future efforts should consider integrating effective cloud filtering techniques, especially modern approaches such as deep learning.

Another key limitation was the occurrence of false positive detections in agricultural areas (Fig. 4a, d, e, h). This misclassification is primarily due to the spectral similarity between bare or disturbed soil in agricultural fields and actual landslide scars, particularly in steep terrain [8],[28]. The problem becomes more complex in hilly areas dominated by tea plantations and seasonal crop cultivation, where periodic vegetation clearing can mimic landslide features. Similar issues were reported by Notti and others in their study [26]. Similarly, exposed soil surfaces and muddy water surfaces in streams and reservoirs lead to false positives (Fig. 5h, i). Such areas often exhibit spectral or backscatter characteristics similar to those of landslide surfaces, particularly in medium-resolution satellite imagery. Consequently, the models may incorrectly classify these areas as potential landslides.

Such misclassification errors can be minimised by integrating land-use land-cover (LULC) maps and object-based image analysis (OBIA) [55]-[57]. Furthermore, the model performance can be improved by integrating high-resolution satellite imagery and high-resolution DEMs [8],[24],[27].

VI. Conclusion

The current study suggests that all four methods applied were reliable for rapid landslide detection in an inter-area scenario; however, SVM-A-M4 is the best model. Both GTB and CART techniques demonstrated strong transformation capabilities, with GTB-B-M3 performing best. However, both the SVM and RF techniques show reduced model transformability. Finally, due to their strong performance in model transferability, the GTB-B-M4 and CART-B-M3 are recommended for reliable, rapid rainfall-induced landslide detection in Sri Lanka.

References

[1] S. Lee, J. H. Ryu, J. S. Won, and H. J. Park, "Determination and application of the weights for landslide susceptibility mapping using an artificial neural network," Eng. Geol., vol. 71, no. 3–4, pp. 289–302, 2004.

[2] D. Petley, "Global patterns of loss of life from landslides," Geology, vol. 40, no. 10, pp. 927–930, 2012.

[3] P. Singh, V. Maurya, and R. Dwivedi, "Pixel based landslide identification using Landsat 8 and GEE," in Proc. IEEE IGARSS, 2021, pp. 8444–8447.

[4] K. Burrows, O. Marc, and C. Andermann, "Retrieval of monsoon landslide timings with Sentinel-1 reveals the effects of earthquakes and extreme rainfall," Geophys. Res. Lett., vol. 50, no. 16, Art. no. e2023GL104720, 2023.

[5] H. A. Jayathissa, "Combined statistical and dynamic modeling for real-time forecasting of rain-induced landslides in Matara District, Sri Lanka," Ph.D. dissertation, Univ. Tübingen, Germany, 2010.

[6] E. N. C. Perera et al., "Direct impacts of landslides on socio-economic systems: A case study from Aranayake, Sri Lanka," Geoenviron. Disasters, vol. 5, Art. no. 12, 2018.

[7] K. Doerksen et al., "Precipitation-triggered landslide prediction in Nepal using machine learning and deep learning," in Proc. IEEE IGARSS, 2023, pp. 4962–4965.

[8] A. A. Chrysafi et al., "Rapid landslide detection following an extreme rainfall event using remote sensing indices, synthetic aperture radar imagery, and probabilistic methods," Land, vol. 14, no. 1, Art. no. 21, 2024.

[9] M. Prodromou et al., "Rapid landslide mapping using multi-temporal image composites from Sentinel-1 and Sentinel-2 imagery through Google Earth Engine," in Proc. IEEE IGARSS, 2023, pp. 2596–2599.

[10] N. Sharma and M. Saharia, "ML-CASCADE: A machine learning and cloud computing-based tool for rapid and automated mapping of landslides," Landslides, vol. 22, no. 1, pp. 31–43, 2025.

[11] F. Guzzetti et al., "Landslide inventory maps: New tools for an old problem," Earth-Sci. Rev., vol. 112, no. 1–2, pp. 42–66, 2012.

[12] Y. E. Yang, T. T. Yu, and C. Y. Chen, "Automatic detection of landslide impact areas using Google Earth Engine," Terr. Atmos. Ocean. Sci., vol. 35, no. 1, pp. 1–22, 2024.

[13] E. N. C. Perera, D. T. Jayawardana, M. Ranagalage, D. M. S. L. B. Dissanayake, and H. M. D. S. Wijenayaka, "Introduce a framework for landslide risk assessment using geospatial analysis: A case study from Kegalle District, Sri Lanka," Model. Earth Syst. Environ., vol. 6, pp. 2415–2431, 2020.

[14] D. K. M. De Silva, S. S. P. Warnakulasuriya, and S. D. Dharmaratne, "Natural disasters and population impact in Sri Lanka, 2010–2025," 2026.

[15] A. C. Mondini, K. T. Chang, and H. Y. Yin, "Combining multiple change detection indices for mapping landslides triggered by typhoons," Geomorphology, vol. 134, no. 3–4, pp. 440–451, 2011.

[16] A. C. Mondini, "Measures of spatial autocorrelation changes in multitemporal SAR images for event landslides detection," Remote Sens., vol. 9, no. 6, Art. no. 554, 2017.

[17] A. J. Ganerød et al., "Automating global landslide detection with heterogeneous ensemble deep-learning classification," Remote Sens. Appl., vol. 36, Art. no. 101384, 2024.

[18] W. Wu et al., "Landslide susceptibility using GEE," Remote Sens., vol. 14, no. 18, Art. no. 4662, 2022.

[19] S. Peters et al., "Detecting coseismic landslides in GEE," Remote Sens., vol. 16, no. 10, Art. no. 1722, 2024.

[20] K. Yang et al., "Dynamic hazard assessment using GBDT," Water, vol. 16, no. 12, Art. no. 1638, 2024.

[21] M. Amani et al., "Google Earth Engine cloud computing platform for remote sensing big data applications: A comprehensive review," IEEE J. Sel. Topics Appl. Earth Obs. Remote Sens., vol. 13, pp. 5326–5350, 2020.

[22] H. F. Ilmy, M. R. Darminto, and A. Widodo, "Application of machine learning on Google Earth Engine to produce landslide susceptibility mapping," in IOP Conf. Ser.: Earth Environ. Sci., vol. 731, 2021, Art. no. 012028.

[23] L. Abad et al., "Detecting landslide-dammed lakes on Sentinel-2 imagery," Sci. Total Environ., vol. 820, Art. no. 153335, 2022.

[24] A. L. Handwerger et al., "Generating landslide density heatmaps for rapid detection," Nat. Hazards Earth Syst. Sci., vol. 22, no. 3, pp. 753–773, 2022.

[25] E. Lindsay et al., "Multi-temporal satellite image composites in Google Earth Engine," Remote Sens., vol. 14, no. 10, Art. no. 2301, 2022.

[26] D. Notti et al., "Semi-automatic mapping of shallow landslides using Sentinel-2 images," Nat. Hazards Earth Syst. Sci., vol. 23, no. 7, pp. 2625–2648, 2023.

[27] S. Phakdimek, D. Komori, and T. Chaithong, "Combination of optical and SAR images for detecting landslide scars," Int. J. Remote Sens., vol. 44, no. 11, pp. 3572–3606, 2023.

[28] J. H. Yang et al., "Enhanced detection of landslides," Adv. Climate Change Res., vol. 15, no. 3, pp. 476–489, 2024

[29] M. S. Seneviratne et al., "Landslide susceptibility mapping in Sri Lanka," Eng. Geol., vol. 98, no. 3–4, pp. 140–154, 2008.

[30] G. Y. Jayasinghe et al., "Landslide hazard assessment in mountainous regions of Sri Lanka," Int. J. Disaster Risk Reduct., vol. 19, pp. 1–12, 2016.

[31] K. L. W. I. Gunathilake et al., "Living with landslide risks," in Rebuilding Communities After Displacement. Springer, 2023, pp. 145–163.

[32] Q. Tang et al., "Estimation of landslide hazards in Aranayake," Landslides, vol. 17, pp. 1727–1738, 2020.

[33] G. J. M. S. R. Jayasinghe et al., "Landslide susceptibility assessment using statistical models," Ceylon J. Sci., vol. 46, no. 4, pp. 19–28, 2017.

[34] M. A. S. Perera, "Machine learning approach for landslide susceptibility modeling," M.S. thesis, Univ. Moratuwa, Sri Lanka, 2021.

[35] D. Jayathilake and D. Munasinghe, "Quantitative landslide risk assessment," in NBRO Symp., Colombo, 2015, pp. 25–34.

[36] R. M. S. Bandara and P. Jayasingha, "Landslide disaster risk reduction strategies," Geosci. Res., vol. 3, pp. 21–27, 2018.

[37] H. Hemasinghe et al., "Landslide susceptibility mapping using logistic regression," Procedia Eng., vol. 212, pp. 1046–1053, 2018.

[38] B. W. G. I. D. Gunarathna et al., "Impact of land use on landslides," Bhumi J., vol. 6, no. 2, pp. 1–16, 2018.

[39] H. S. Lasantha and A. M. R. G. Athapaththu, "Slope stability assessment in Sri Lanka," Bull. Eng. Geol. Environ., vol. 83, no. 2, Art. no. 54, 2024.

[40] H. S. Lasantha and A. M. R. G. Athapaththu, "Multidisciplinary slope stability assessment," Geotech. Geol. Eng., vol. 42, no. 7, pp. 6027–6050, 2024.

[41] S. Neranjan et al., “Geometrical variation analysis of landslides,” Remote Sens., vol. 16, no. 10, Art. no. 1757, 2024.

[42] T. Pushpakumara et al., “Predicting landslide-prone areas using GIS,” Univ. Moratuwa, 2003.

[43] A. K. R. N. Ranasinghe et al., “Integration of radar and optical remote sensing,” in Proc. ACRS, 2016, pp. 1363–1372.

[44] A. K. R. N. Ranasinghe et al., “Radar-derived factors in landslide analysis,” Nat. Hazards Earth Syst. Sci., vol. 19, no. 8, pp. 1881–1893, 2019.

[45] N. Alahacoon et al., “Flood hazard mapping in Sri Lanka,” Remote Sens., vol. 10, no. 3, Art. no. 448, 2018.

[46] W. D. K. V. Nandasena et al., “Monitoring invasive species,” Environ. Monit. Assess., vol. 195, no. 2, Art. no. 347, 2023.

[47] D. Jayasekara, H. M. B. S. Herath, and N. Gangodawila, “Application of AI-based modelling and remote sensing to assess inselberg habitats in Gampaha District, Sri Lanka,” in Proc. Asian Conf. Remote Sens. (ACRS), 2024, pp. 1–26.

[48] NBRO, “Landslide damage assessment and drone survey,” Colombo, Sri Lanka, 2017.

[49] N. S. Watte Vidanelage and W. A. K. Indika Wanasingha, “Validated high resolution (12.5 m) DEM for Sri Lanka,” Mendeley Data, vol. V1, 2024, doi: 10.17632/hzf2fpndpt.1.

[50] N. Gorelick, M. Hancher, M. Dixon, S. Ilyushchenko, D. Thau, and R. Moore, “Google Earth Engine: Planetary-scale geospatial analysis for everyone,” Remote Sens. Environ., vol. 202, pp. 18–27, 2017.

[51] D. Lu, P. Mausel, E. Brondizio, and E. Moran, “Change detection techniques,” Int. J. Remote Sens., vol. 25, no. 12, pp. 2365–2401, 2004.

[52] F. Furukawa, J. Morimoto, N. Yoshimura, and M. Kaneko, “Comparison of conventional change detection methodologies using high-resolution imagery to find forest damage caused by typhoons,” Remote Sens., vol. 12, no. 19, p. 3242, 2020.

[53] A. R. Huete, “A soil-adjusted vegetation index (SAVI),” Remote Sens. Environ., vol. 25, no. 3, pp. 295–309, 1988.

[54] A. C. Mondini, M. Santangelo, M. Rocchetti, E. Rossetto, A. Manconi, and O. Monserrat, “Sentinel-1 SAR amplitude imagery for rapid landslide detection,” Remote Sens., vol. 11, no. 7, p. 760, 2019.

[55] T. R. Martha et al., “Spectral and morphometric properties of landslides,” Geomorphology, vol. 116, no. 1–2, pp. 24–36, 2010.

[56] A. Stumpf and N. Kerle, “Object-oriented mapping of landslides,” Remote Sens. Environ., vol. 115, no. 10, pp. 2564–2577, 2011.

[57] B. Adriano et al., “Semiautomatic landslide detection,” Remote Sens., vol. 12, no. 3, Art. no. 561, 2020.